— 16 —

High-accuracy positioning: astrometry

Lennart Lindegren[I]

Abstract

The limiting accuracy for measuring the location of an optical image is set by diffraction and photon noise, i.e., by the dual wave–particle nature of light. A theoretical expression for the limiting accuracy is derived under idealized conditions and generalized to take into account more realistic circumstances, such as additive noise and finite pixel size. Its application is discussed in relation to different space-astrometry techniques including grid modulation, direct imaging, and interferometry.

Advantages of space observations for astrometry

Astrometry is the branch of observational astronomy concerned with the accurate determination of the angular coordinates of celestial bodies, and of the temporal changes in the coordinates caused by effects such as proper motion, parallax, orbital motion, and gravitational light deflection. The uses of such data are numerous and wide-ranging; see, e.g., Turon and Robichon (2006). Although modern astrometric techniques embrace the whole electromagnetic spectrum from γ-ray observations (Taff 1988) to radio interferometry (Fomalont 2005), only optical and near-infrared measurements from space are considered here. The launch, in 1989, of the ESA space-astrometry satellite *Hipparcos* (Perryman, ESA 1997) revolutionized optical astrometry and firmly demonstrated the advantages of a space platform for such measurements (Perryman 2009). At about the same time, high-accuracy astrometric observations were started with *HST* (Benedict et al 1994, 2003). The ESA *Gaia* mission (Perryman 2005) is the most ambitious space-astrometry project currently under development; it will survey some 10^9 objects brighter than 20th magnitude at angular accuracies in the 10 µas to 300 µas range. The proposed missions *SIM PlanetQuest* (Nemati 2006; Unwin et al 2008) and *SIM-Lite* (Shao and Nemati 2009) are pointed interferometers aiming at accuracies down to 1 μas or less, albeit for a smaller number of targets ($\simeq 10^4$).

The advantages of space for optical astrometric observations were not universally recognized at the time when *Hipparcos* was under discussion. After all, such measurements had for centuries been made from the ground, with steadily increasing precision and significant potential for improvement (Connes 1979). With the

[I]Lund Observatory, Lund, Sweden

hindsight of the *Hipparcos* experience, the advantages of space can briefly be stated as follows:

- The absence of an atmosphere eliminates the systematic and random effects of refraction and turbulence (seeing).
- Weightlessness eliminates the differential mechanical deformation of the instrument as it is pointed in different directions.
- With proper design of the instrument and spacecraft, space may provide a thermally and mechanically very stable environment.
- At any time, nearly the whole sky is simultaneously accessible from a single observatory, and over a few months the whole sky is accessible.

The last point is perhaps the least obvious advantage, but it is in fact essential for accurate calibration of the instrument and for the determination of absolute parallaxes and an internally consistent global reference frame.

The basic astrometric measurement quantifies the observed direction of a light ray in terms of detector coordinates. These could be the location of the image centre (expressed in pixels and fractions thereof) at a given time, or the phase of a fringe pattern (for an interferometer). Their astrometric interpretation involves a series of transformations, taking into account the geometric calibration of the instrument, its orientation in space (attitude), and the relation between the observed direction and celestial coordinates in some standard reference frame. The first two transformations are highly mission-specific and will not be further considered here, while the last one requires a general-relativistic framework, e.g., as described by Klioner (2003). Only the basic directional observation, in terms of detector coordinates, is presently discussed.

Optical image formation and positional accuracy

The fundamental limit

The limiting positional accuracy (i.e., for an 'ideal' detector) can be derived from elementary considerations of noise and resolution (Falconi 1964; Lindegren 1978). Ultimately, the limit is set by the dual wave–particle nature of light, i.e., by diffraction and photon noise.

With a proper choice of coordinate axes, measurements in orthogonal directions are uncorrelated and it suffices to consider one-dimensional measurements along an axis denoted x (in linear measure) or ξ (in angular measure). Lindegren (2005) showed that a limiting expression for the standard deviation of the angular position ξ can be derived directly from the Heisenberg uncertainty principle, namely

$$\sigma_\xi \geq \frac{\lambda}{4\,\pi\,\Delta x\sqrt{N}} \quad , \tag{16.1}$$

where λ is the wavelength of the radiation, N the number of photons detected, and Δx the root-mean-square (rms) extension of the telescope entrance pupil in the x direction (for example, $\Delta x = D/4$ for a circular pupil of diameter D, $\Delta x = L/\sqrt{12}$

for a rectangular pupil of size L in the x direction, and $\Delta x = B/2$ for a two-element interferometer with projected baseline B in the x direction). Equation 16.1 gives a lower bound which could in principle be approached under ideal circumstances — aberration-free imaging, no background illumination, etc. — and is therefore a useful reference quantity.

Limiting accuracy from diffraction optics

In the Fraunhofer approximation (Born and Wolf 1999) the monochromatic point-spread function (PSF) is

$$P_\lambda(\xi,\eta) = \frac{1}{\lambda^2 A}\left|\iint_{\mathcal{P}} \exp\Big[-\mathrm{i}\,(2\,\pi/\lambda)\big(x\xi + y\eta + W(x,y)\big)\Big]\,\mathrm{d}x\,\mathrm{d}y\right|^2 \qquad (16.2)$$

where (x, y) are linear coordinates in the telescope pupil $\mathcal{P}$, (ξ, η) the corresponding angular coordinates in the image plane, $W(x, y)$ the wavefront uncertainty of the telescope, and A the area of the pupil.

Equation 16.2 is normalized to $\iint_{-\infty}^{+\infty} P_\lambda(\xi,\eta)\mathrm{d}\xi\mathrm{d}\eta = 1$, and therefore gives the probability density function (pdf) for photon detection at $\alpha = \alpha_0 + \xi$, $\beta = \beta_0 + \eta$, given quasi-monochromatic radiation of wavelength λ with the optical centre at (α_0, β_0). Assuming a stationary image with no background illumination and an ideal detector registering the precise coordinates (α_i, β_i) of N photon detection events, the optical centre can be estimated by maximizing the log-likelihood function

$$\ell(\alpha_0,\beta_0) = \sum_{i=1}^{N} \ln P_\lambda(\alpha_i - \alpha_0, \beta_i - \beta_0) \quad . \qquad (16.3)$$

The covariance of the resulting maximum-likelihood estimate $(\hat{\alpha}_0, \hat{\beta}_0)$ can be obtained by means of the Cramér–Rao bound (Stuart et al 1998),

$$\mathrm{Cov}\begin{bmatrix}\hat{\alpha}_0\\ \hat{\beta}_0\end{bmatrix} \geq \begin{bmatrix} \mathrm{E}\left(\frac{\partial\ell}{\partial\alpha_0}\frac{\partial\ell}{\partial\alpha_0}\right) & \mathrm{E}\left(\frac{\partial\ell}{\partial\alpha_0}\frac{\partial\ell}{\partial\beta_0}\right)\\ \mathrm{E}\left(\frac{\partial\ell}{\partial\beta_0}\frac{\partial\ell}{\partial\alpha_0}\right) & \mathrm{E}\left(\frac{\partial\ell}{\partial\beta_0}\frac{\partial\ell}{\partial\beta_0}\right)\end{bmatrix}^{-1} \quad , \qquad (16.4)$$

where E is the expectation operator. Using Equation 16.3 and introducing $U_\lambda(\xi,\eta) = 2\sqrt{P_\lambda(\xi,\eta)}$, the first matrix element on the right-hand side of Equation 16.4 can be written

$$\mathrm{E}\left(\frac{\partial\ell}{\partial\alpha_0}\right)^2 = N\iint_{-\infty}^{+\infty}\left(\frac{\partial P_\lambda}{\partial\xi}\right)^2\frac{\mathrm{d}\xi\,\mathrm{d}\eta}{P_\lambda(\xi,\eta)} = N\iint_{-\infty}^{+\infty}\left(\frac{\partial U_\lambda}{\partial\xi}\right)^2\mathrm{d}\xi\,\mathrm{d}\eta \qquad (16.5)$$

and similarly for the other matrix elements.

The above expressions are valid for arbitrary wavefront aberrations and pupil shapes. Consider now the special case of an aberration-free system, $W(x, y) = 0$, whose pupil is symmetric with respect to both axes. The Fourier double integral in Equation 16.2 is then real and

$$\frac{\partial U_\lambda}{\partial\xi} = \frac{\mathrm{i}\,4\,\pi}{\lambda^2\sqrt{A}}\iint_{\mathcal{P}}\exp\big[-\mathrm{i}\,(2\pi/\lambda)(x\xi + y\eta)\big]\,x\,\mathrm{d}x\,\mathrm{d}y \qquad (16.6)$$

etc. Applying Parseval's identity, and using the symmetry of the pupil, gives

$$\iint_{-\infty}^{+\infty} \left(\frac{\partial U_\lambda}{\partial \xi}\right)^2 \mathrm{d}\xi\,\mathrm{d}\eta = \frac{16\pi^2\Delta x^2}{\lambda^2} \quad , \tag{16.7}$$

with a corresponding expression in y and η, and zero cross term. The matrix in Equation 16.4 is therefore diagonal, and the Cramér–Rao bound gives the variances

$$\mathrm{Var}(\xi) \geq \frac{\lambda^2}{16\pi^2\Delta x^2 N}\,, \qquad \mathrm{Var}(\eta) \geq \frac{\lambda^2}{16\pi^2\Delta y^2 N} \tag{16.8}$$

in complete agreement with Equation 16.1. For notational convenience, (ξ, η) were here re-introduced for the estimated image centre, instead of $(\hat{\alpha}_0, \hat{\beta}_0)$.

Generalizations

Based on the first equality in Equation 16.5, a number of generalizations can now be introduced. First, it is noted that $P_\lambda(\xi, \eta)$ in Equation 16.5 may include arbitrary wavefront aberrations via Equation 16.2, although the various integrals must then be evaluated numerically. In general, aberrations result in a reduction of the overall PSF slopes in 16.5 and consequently in an increased variance of the estimated centroid coordinate.

Second, for real instruments operating in a finite wavelength band, the monochromatic PSF, $P_\lambda(\xi, \eta)$, must be replaced by the polychromatic PSF

$$P(\xi, \eta) = \frac{\int_0^\infty T_\lambda Q_\lambda P_\lambda(\xi, \eta)\,\mathrm{d}\lambda}{\int_0^\infty T_\lambda Q_\lambda\,\mathrm{d}\lambda} \quad , \tag{16.9}$$

where T_λ is the total optical transmittance and Q_λ the detector quantum efficiency.

Third, further degradation of the image caused by the detector may be included by replacing the optical PSF by an 'effective PSF' (ePSF, Anderson and King 2000)

$$\widetilde{P}(\xi, \eta) = P(\xi, \eta) * P_{\mathrm{pixel}} * P_{\mathrm{diffusion}} * P_{\mathrm{motion}} * \cdots \tag{16.10}$$

obtained through convolution with a series of probability density functions representing the pixel response function, the diffusion of photoelectrons in the CCD silicon substrate, the motion of the image during the exposure, etc. (cf., Page 285).

Finally, let $S(\xi, \eta) = N\widetilde{P}(\xi, \eta)$ be the expected density of stellar photon detections per unit area of the detector and b the expected background density, then

$$\sigma_\xi \geq \left[\iint_{-\infty}^{+\infty} \frac{1}{S(\xi, \eta) + b} \left(\frac{\partial S}{\partial \xi}\right)^2 \mathrm{d}\xi\,\mathrm{d}\eta\right]^{-1/2} \quad . \tag{16.11}$$

Here, b can be taken to represent all constant noise sources, including sky background, detector dark counts, and CCD readout noise (an rms readout noise of r electrons per pixel is equivalent to an increase of the background level by r^2 counts per pixel).

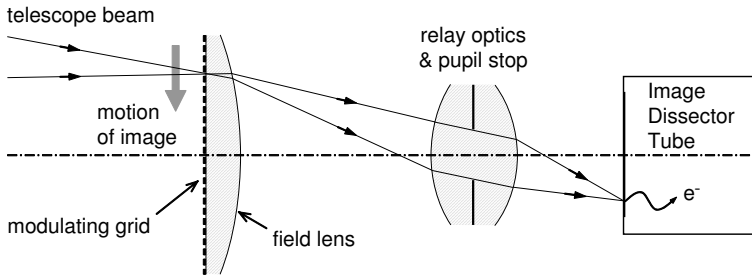

Figure 16.1: Positional encoder for *Hipparcos*: a modulating grid consisting of 2688 transparent slits, covering the central $0.9^\circ \times 0.9^\circ$ of the telescope field of view.

The methodology outlined above allows an estimate of the precision of centroiding on a detected image affected by optical aberrations, sky background, pixelization and other detector imperfections including readout noise. The lower bound in Equation 16.11 can be computed without specifying the centroiding algorithm, and from estimation theory it can be deduced that a good centroiding algorithm (e.g., based on the maximum likelihood method) should come close to this limit, at least when N is not too small. The lower bound is therefore extremely useful for evaluation and optimization purposes, and as an absolute standard for the performance of practical centroiding algorithms.

Example 1: the modulating grid of *Hipparcos*

When the *Hipparcos* satellite design was finalized in the mid-1980s, CCDs were not considered sufficiently stable, or technologically mature, for space-astrometry applications. The solution adopted for *Hipparcos* was to encode the positions of stellar images by means of a highly accurate mask, or modulating grid, occupying the focal surface in front of a photon-counting detector (Figure 16.1). Light modulation was effected through the continuous rotation of the instrument at a nominal speed of $168.75'' \ \mathrm{s}^{-1}$. The resulting periodic variation of the transmitted intensity (Figure 16.2) could be accurately modelled by a truncated Fourier series, which for single stars gave the following expression for the photon-count density:

$$S(\xi) = F\big[1 + M_1 \cos(2\pi\xi/s) + M_2 \cos(4\pi\xi/s + \epsilon)\big] \quad . \tag{16.12}$$

Here, ξ is the instantaneous angular coordinate of the image, s the grid period, F the mean stellar count rate (in counts per grid period), and $M_1 \simeq 0.71$, $M_2 \simeq 0.25$ and $\epsilon \simeq 10^\circ$ are instrument 'constants' that have to be accurately calibrated. The grid period $s \simeq 1.2''$ was chosen to give negligible third harmonic in the Fourier series expansion of the detector signal; indeed, the third and higher harmonics are strictly zero for $\lambda > sD/3 \simeq 560$ nm, where $D = 0.29$ m is the diameter of the *Hipparcos* entrance pupil. The slit width $\simeq 0.46''$ was optimized for positional accuracy, taking into account the theoretically predicted variation of F, M_1 and M_2 with the slit width.

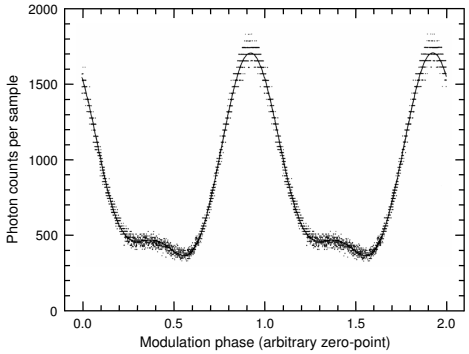

Figure 16.2: Photon counts for a bright (magnitude $\simeq$ 2) star observed with the *Hipparcos* encoder (Fig. 16.1). 2560 consecutive samples are plotted versus the modulation phase (modulo the modulation period). The curve is the fitted Equation 16.12. The discretization prominent for large counts is due to the semi-logarithmic data-compression algorithm coding the counts into 8-bit words.

The performance of the *Hipparcos* positional encoder can be evaluated by inserting Equation 16.12 into Equation 16.11, ignoring the perpendicular coordinate (η). Assuming negligible background ($b \ll F$) and the quoted values for M_1, M_2 and ϵ, we find $(\sigma_\xi)_{\rm Hipp} \simeq 0.330'' N^{-1/2}$, where $N = Ft$ is the total number of photons registered over t modulation periods. This is in fair agreement with values derived from a re-analysis of the *Hipparcos* raw data (van Leeuwen 2007). For comparison, the theoretical limit 16.1 gives $(\sigma_\xi)_{\rm theory} \simeq 0.125'' N^{-1/2}$, assuming $\lambda_{\rm eff} \simeq 550$ nm. Considering in addition that only one third of the photons are transmitted by the grid and relayed to the detector, one can conclude that the grid-modulation technique is not very efficient in absolute terms.

Example 2: CCD imaging for space astrometry

Compared with the *Hipparcos* detection system described above, CCDs have huge advantages in terms of quantum efficiency, broad wavelength coverage, no light loss due to a modulating device, and the possibility to observe many objects simultaneously (Lindegren 2005). The capability of CCDs for high-accuracy differential astrometry from space is well demonstrated using images from the *HST* Wide Field and Planetary Camera 2 (WFPC2) (Anderson and King 2000, 2003) and Advanced Camera for Surveys/Wide Field Channel (ACS/WFC) (Anderson and King 2006), although these cameras were not specifically designed for astrometry. Future space-astrometry missions will use CCDs for direct imaging in drift-scanning mode (*Gaia*) and for fringe tracking in interferometers (e.g., *SIM PlanetQuest*). These instruments represent very different modes of utilizing CCDs for space astrometry.

Direct imaging in pointing mode

High-accuracy astrometry in a field of any appreciable size requires that the image centroids are located to within a small fraction of the pixel size. For example, 1 mas corresponds to about 0.02 pixel both in the WFPC2 and the ACS/WFC. This is in principle not a problem if the image is well-sampled and recorded with sufficient signal-to-noise ratio. The sampling theorem (e.g., Wall and Jenkins 2003) provides a useful rule-of-thumb estimate of the maximum desired pixel size p in terms of the telescope aperture and effective wavelength:

$$p \leq p_{\rm crit} \equiv \frac{\lambda_{\rm eff}}{2\,D} \quad . \tag{16.13}$$

For the *HST* ($D = 2.4$ m) in visual light ($\lambda_{\rm eff} \simeq 550$ nm) this gives $p \leq 24$ mas, or about half the actual pixel size for WFPC2 and ACS/WFC. However, undersampling is not by itself a problem for accurate positioning, provided that the underlying image is simple enough (e.g., consisting of a small number of point sources). A more useful, quantitative criterion can be derived in terms of the limiting positional accuracy as function of p, using Equations 16.10 and 16.11 with the idealized (boxcar) pixel response function

$$P_{\rm pixel}(\xi,\eta) = \begin{cases} 1/p^2 & \text{if } |\xi| < p/2 \text{ and } |\eta| < p/2 \\ 0 & \text{otherwise} \end{cases} \quad . \tag{16.14}$$

Figure 16.3 shows the relative increase in σ_ξ as function of $p/p_{\rm crit}$ for an aberration-free optical system with circular pupil. The effect of the pixelization depends both on the relative bandwidth of the radiation and the level of background noise; three different cases are shown in the diagram. It is seen that the degradation is quite gradual with increasing pixel size, with no specific significance attached to the critical sampling. Thus, some degradation is observed already for well-sampled images ($p/p_{\rm crit} < 1$), while severely undersampled images could still be useful for astrometry. For the WFPC2 and ACS/WFC cameras ($p/p_{\rm crit} \simeq 2$) the pixelization is expected to increase the relative centroiding uncertainty by some 50 %. Optical aberrations and charge diffusion, neglected in this discussion, will increase the uncertainty by some further factor.

To achieve the highly accurate centroiding actually in practice is, however, a different matter. Simplistic centroiding algorithms such as using the moments of the light distribution (Howell 2000) are totally inadequate both in terms of precision and systematic uncertainties. Anderson and King (2000) have demonstrated that the key to successful astrometry with the *HST* cameras is to make an extremely accurate calibration of the ePSF, and subsequently use this for fitting to the observed CCD data. It should be noted that the commonly employed (sub-pixel) dithering techniques (Fruchter and Hook 2002) do not eliminate the information-loss caused by the undersampling, but greatly facilitate the accurate determination of the ePSF.

All CCD detectors used on the *HST* instruments suffer from charge transfer inefficiency (CTI), i.e., from the fact that the transfer of charge from one pixel to the next is not perfect. The measurable effects include loss of flux and systematic centroid shifts depending on (among other things) the position on the chip, the size

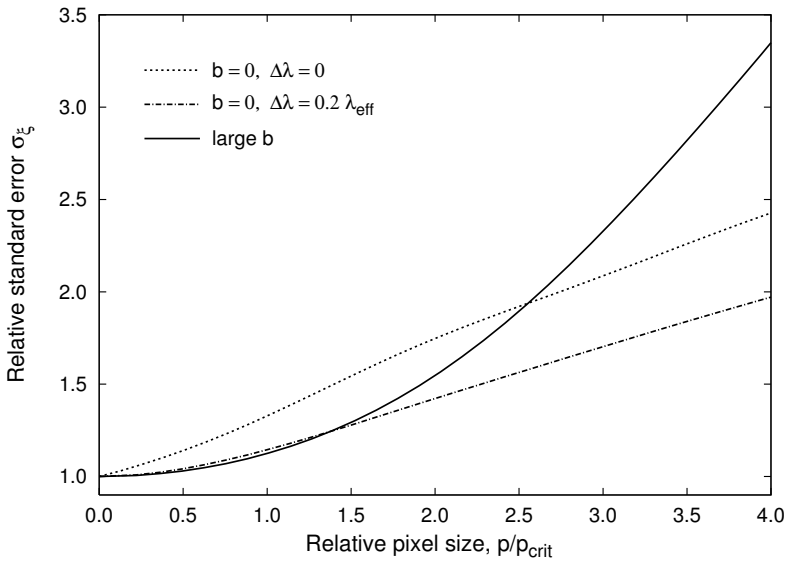

Figure 16.3: Theoretical degradation of the centroiding precision from the pixelization of an aberration-free diffraction image (circular pupil), as function of pixel size. Dashed curves are for no background ($b = 0$) and different bandwidths $\Delta\lambda$; the solid curve is for the large-background case ($b \gg NA/\lambda_{\rm eff}^2$), where the effect is nearly independent of $\Delta\lambda$.

of the signal, and the background level (Goudfrooij et al 2006; Kozhurina-Platais et al 2007).

Direct imaging in drift-scanning mode

Fast-moving objects can be imaged by operating the CCD in the time, delay and integrate (TDI) mode, also known as drift-scanning. The charges are clocked along the CCD columns at the same (average) speed as the motion of the optical image. The integration time is set by the time it takes the object to move across the CCD. The use of TDI imaging in astronomy is well-known from ground-based programmes such as the Sloan Digital Sky Survey (Gunn et al 1998).

The *Gaia* instrument will use a mosaic of 76 CCDs (SM and AF in Figure 16.4) to detect and record the images of point-like objects traversing the focal plane as a result of the continuous rotation of the satellite at $60'' \ {\rm s}^{-1}$. Additional CCDs are used for spectrophotometric and spectroscopic characterization of the objects. All detectors are large-size (45 mm $\times$ 59 mm), back-illuminated CCDs operated in TDI mode, providing a maximum integration time of 4.4 s per CCD.

A single CCD detector sweeps a strip of the sky of the same width as the CCD but in principle indefinitely long. By slowly changing the direction of *Gaia*'s spin axis according to a well-defined 'scanning law', the strips from all the CCDs provide multiple coverage of the whole celestial sphere in a period of six months. Two optical fields of view, separated by a 'basic angle' of 106.5° on the sky, are

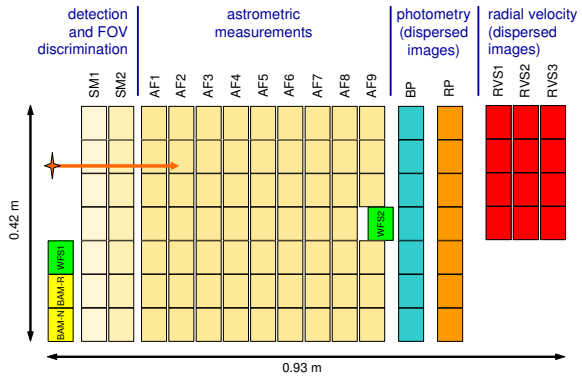

Figure 16.4: Layout of CCDs in the focal plane of *Gaia* (Lindegren et al 2008). Images travel from left to right, crossing in turn the skymappers (SM), astrometric field (AF), blue photometer (BP), red photometer (RP), and the radial-velocity spectrometer (RVS). Also shown are CCDs for the basic-angle monitor (BAM) and wavefront sensors (WFS).

superposed on the single focal plane, although the two skymappers (SM) view the fields separately. This measurement principle means that the centroiding accuracy must be optimized in the along-scan direction (say, ξ), while this requirement is much relaxed in the across-scan direction (Lindegren 2005). The entrance pupils for the *Gaia* telescopes are consequently rectangular (1.45 m $\times$ 0.5 m) with the longer dimension (L) along x, and the pixel size 10 μm $\times$ 30 μm was chosen to match the resulting diffraction image, with the smaller dimension (p) along ξ. Further on-chip binning is employed in the across-scan (η) direction during the readout of the CCDs in the astrometric field.

Since the elementary astrometric observations are thus basically one-dimensional, the relevant response function is the effective line spread function (eLSF), i.e., the marginal density of the ePSF:

$$\widetilde{P}(\xi) = \int_{-\infty}^{+\infty} \widetilde{P}(\xi,\eta)\,\mathrm{d}\eta \quad . \tag{16.15}$$

The theoretical centroiding accuracy can be estimated from the photon count rate and eLSF in complete analogy with the two-dimensional case. The main difference is that the TDI mode introduces some additional smearing of the eLSF due to the relative motion of the optical image with respect to the transported charges during the exposure. This motion has three main causes: the TDI operation itself (the charges move step-wise, while the optical image is in continuous motion); local mismatch in scale due to optical distortions; and real-time attitude-control errors. The TDI stepping can be modelled, for a four-phase CCD, as a convolution with a rectangular function of width $p/4$. The combined smearing from other causes may be modelled as a convolution with a Gaussian function; the estimated standard width is of order 0.13 p. Charge diffusion causes additional, wavelength-dependent smearing (Janesick 2001).

The combination of linear pixel size ($p = 10$ μm), pupil size (L) and focal length ($F = 35$ m) chosen for *Gaia* means that the stellar images are undersampled for $\lambda < 2\,p\,L/F \simeq 830$ nm. (The total wavelength coverage is about 400 nm to 1000 nm.) This results in some accuracy degradation similar to Figure 16.3. In reality the pupil size and the linear dimensions of the focal plane are determined by practical and budgetary constraints depending on volume, mass, power dissipation, and technical complexity. The chosen focal length is nearly optimal in this respect: a longer focal length would certainly reduce the undersampling factor and hence the astrometric centroiding uncertainty per unit integration time, but it would also decrease the integration time per CCD as well as the mean number of observations per object for a given size of the focal plane. The average accumulated integration time per object scales as F^{-2}, so that the photon-noise factor on the resulting uncertainty is proportional to F. As a result, the optimum F corresponds to slightly undersampled images.

An important consideration for the performance of the *Gaia* mission is the possible accuracy degradation caused by radiation damage to the CCDs (Lindegren et al 2008), i.e., the previously mentioned CTI effects. Extensive laboratory tests on irradiated CCDs show significant charge loss and centroid shifts both along and across the scan. The effects are very reproducible, and therefore possible to calibrate, but their accurate modelling remains a challenging aspect of the *Gaia* data analysis.

Example 3: interferometry

Astrometric measurements made with space interferometers will benefit from the increased angular resolution obtained with baselines B much longer than any single telescope aperture, cf., Equation 16.1 where $\Delta x = B/2$ in this case. For example, the planned *SIM PlanetQuest* has $B \simeq 9$ m, allowing the angles between bright (< 10 mag) target stars to be measured to a precision of $\simeq 1$ μas (individual measurements in the narrow-angle mode). This very high precision is primarily motivated by the search for terrestrial planets (Shao 2006).

The condition for centroiding on an object is that the optical path length from the incident plane wavefront to the detector is the same in the two interferometer arms, i.e., that the optical path difference (OPD) is zero to within a fraction of a wavelength, yielding constructive interference at the beam combiner. The delay in one of the arms is first adjusted until fringes are observed. Then, in order to determine the precise delay corresponding to no OPD, a saw-tooth modulation of the OPD is introduced and the intensity is measured as function of the delay. In the monochromatic approximation the measured intensity at OPD position u can be written (Meier and Folkner 2003)

$$S(u) = F\left[1 + V\cos(k\,u + \phi)\right] \quad , \tag{16.16}$$

where the parameters are the mean flux F (per unit time), fringe visibility (contrast) V, wave number k, and phase ϕ. Least-squares fitting of this fringe model to the CCD pixel values as function of u gives an estimate of all four parameters. The

limiting accuracy of the phase determination is readily derived analytically from 16.11, viz.

$$\sigma_\phi \geq \left[\left(1 - \sqrt{1 - \left(\frac{FV}{F+b} \right)^2} \right) (F+b)\, t \right]^{-1/2} \quad , \tag{16.17}$$

where t is the integration time and b the background, including CCD readout noise as previously discussed. For projected baseline B the phase uncertainty σ_ϕ translates to the uncertainty in angular position $\sigma_\theta = (\sigma_\phi/2\pi)(\lambda_{\rm eff}/B)$. With $N = Ft$ denoting the total number of detected photons, and assuming $b \ll F$, it is seen that

$$\sigma_\theta \geq \frac{\lambda_{\rm eff}}{2\pi B\sqrt{N}} \left(1 - \sqrt{1 - V^2} \right)^{-1/2} \quad . \tag{16.18}$$

Compared with Equation 16.1, with $\Delta x = B/2$, this uncertainty is a factor $(1 - \sqrt{1-V^2})^{-1/2} \geq 1$ greater, with equality for $V = 1$. Thus, provided the fringe contrast is high and the detector noise small, the performance of the astrometric interferometer in terms of the internal phase uncertainty may approach that of an ideal instrument.

Conclusions

Observations from space offer unique advantages for high-accuracy positioning, or astrometry. In particular, the absence of any atmosphere allows diffraction-limited performance of imaging and interferometric devices. In the photon-counting regime the best possible positional accuracy of such devices can be evaluated from simple and general statistical considerations, as illustrated by the specific examples in this chapter. It can be argued that the actual performance of any real, well-designed experiment should approach this theoretical limit to within a small numerical factor.

Bibliography

Anderson J, King IR (2000) Toward high-precision astrometry with WFPC2. I. Deriving an accurate point-spread function. Publ Astr Soc Pac 112:1360–1382

Anderson J, King IR (2003) An improved distortion solution for the *Hubble* Space Telescope's WFPC2. Publ Astr Soc Pac 115:113–131

Anderson J, King IR (2006) PSFs, photometry, and astrometry for the ACS/WFC. Space Telescope Science Institute, Instrument Science Report ACS 2006-01

Benedict GF, McArthur B, Nelan E (plus 11 authors) (1994) Astrometry with Hubble Space Telescope fine guidance sensor number 3: Position-mode stability and precision. Publ Astr Soc Pac 106:327–336

Benedict GF, McArthur BE, Fredrick LW (plus 17 authors) (2003) Astrometry with the Hubble Space Telescope: A parallax of the central star of the Planetary Nebula NGC 6853. Astron J 126:2549–2556

Born M, Wolf E (1999) Principles of optics: Electromagnetic theory of propagation, interference and diffraction of light (7th ed.). Cambridge: Cambridge University Press
Connes P (1979) Should we go to space for parallaxes? Astron Astrophys 71:L1–L4
Falconi O (1964) Maximum sensitivities of optical direction and twist measuring instruments. J Opt Soc Am 54:1315–1320
Fomalont EB (2005) Radio astrometry: Present status and future. ASP Conf Ser 338:335–342
Fruchter AS, Hook RN (2002) Drizzle: a method for the linear reconstruction of undersampled images. Publ Astr Soc Pac 114:144–152
Goudfrooij P, Bohlin RC, Maíz-Apellániz J, Kimble RA (2006) Empirical corrections for charge transfer inefficiency and associated centroid shifts for STIS CCD observations. Publ Astr Soc Pac 118:1455–1473
Gunn JE, Carr M, Rockosi C (plus 37 authors) (1998) The Sloan digital sky survey photometric camera. Astron J 116:3040–3081
Howell SB (2000) Handbook of CCD astronomy. Cambridge: Cambridge University Press
Janesick JR (2001) Scientific charge-coupled devices. SPIE monograph PM 83. Bellingham, WA: SPIE Optical Engineering Press
Klioner SA (2003) A practical relativistic model for microarcsecond astrometry in space. Astron J 125:1580–1597
Kozhurina-Platais V, Goudfrooij, Puzia TH (2007) ACS/WFC: Differential CTE corrections for photometry and astronomy from non-drizzled images. Space Telescope Science Institute, Instrument Science Report ACS 2007-04
Lindegren L (1978) Photoelectric astrometry — A comparison of methods for precise image location. IAU Coll 48: Modern Astrometry, pp 197–217
Lindegren L (2005) The astrometric instrument of *Gaia*: Principles. ESA SP-576:29–34
Lindegren L, Babusiaux C, Bailer-Jones C (plus ten authors) (2008) The Gaia mission: science, organization and present status. IAU Symp. No. 248, pp 217–223
Meier DL, Folkner WM (2003) SIMsim: an end-to-end simulation of SIM. Proc SPIE 4852:131–142
Nemati B (2006) *SIM PlanetQuest*: status and recent progress. Proc SPIE 6268:62680Q-1–10
Perryman MAC, ESA (1997) The Hipparcos and Tycho Catalogues. ESA SP-1200
Perryman MAC (2005) Overview of the *Gaia* mission. ASP Conf Ser 338:3–14
Perryman MAC (2009) Astronomical applications of astrometry: A review based on ten years of exploitation of the *Hipparcos* satellite data. Cambridge: Cambridge University Press
Shao M (2006) Search for terrestrial planets with *SIM PlanetQuest*. Proc SPIE 6268:62681Z-1–6
Shao M, Nemati B (2009) Sub-microarcsecond astrometry with *SIM-Lite*: A testbed-based performance assessment. Publ Astr Soc Pac 121:41–44
Stuart A, Ord JK, Arnold S (1998) Kendall's Advanced Theory of Statistics, Volume 2A: Classical Inference and the Linear Model (6th ed.). London: Hodder Arnold

Taff LG (1988) Gamma-ray burst astrometry. Astrophys J 326:1032–1035
Turon C, Robichon N (2006) Astrometric surveys. Mem Soc Astron Italiana 77:1073–1080
Unwin SC, Shao M, Tanner AM (plus 33 authors) (2008) Taking the Measure of the Universe: Precision astrometry with *SIM PlanetQuest*. Publ Astr Soc Pac 120:38–88
van Leeuwen F (2007) *Hipparcos*, the new reduction of the raw data. Astrophysics and Space Science Library Vol. 350
Wall JV, Jenkins CR (2003) Practical statistics for astronomers. Princeton Series in Astrophysics. Cambridge: Cambridge University Press